Airborne Measurements of the Wavenumber Spectra of Ocean Surface Waves. Part I: Spectral Slope and Dimensionless Spectral Coefficient*

PAUL A. HWANG AND DAVID W. WANG

Oceanography Division, Naval Research Laboratory, Stennis Space Center, Mississippi

EDWARD J. WALSH+ AND WILLIAM B. KRABILL

NASA/GFSC/WFF, Wallops Island, Virginia

ROBERT N. SWIFT

EG&G, WFF, Wallops Island, Virginia

(Manuscript received 12 May 1999, in final form 15 December 1999)

ABSTRACT

An airborne scanning lidar system acquires 3D spatial topography of ocean surface waves. From the spatial data, wavenumber spectra are computed directly. The spectral analyses of two distinctively different wave fields are presented. The first one is a quasi-steady wave field under active wind generation, and the second one is a decaying wave field following a slackening of the wind field. Subtle differences in different representations of the one-dimensional spectrum (omnidirectional, marginal, and traverse) are illustrated. The spectral properties in terms of the dimensionless spectral coefficient and spectral slope in the equilibrium range are investigated using the wavenumber spectra directly computed from the 3D topography of the ocean surface. The results are in excellent agreement with existing data. The rapid data acquisition afforded by an airborne system provides an enhanced capability for studying the spatial variation of a wave field with minimal temporal changes in the environmental forcing conditions. The data of the 3D surface topography are also ideal for the quantitative investigation of the directional properties of a random wave field.

1. Introduction

The study of the directionality of a random wave field is stimulated by air–sea interactions (e.g., Donelan et al. 1985), nonlinear wave dynamics (e.g., Komen et al. 1984; Banner and Young 1994), or engineering applications (e.g., Forristall and Ewans 1998). Young (1994) and Ewans (1998) have presented detailed comparisons of four established directional distribution models (Mitsuyasu et al. 1975; Hasselmann et al. 1980; Donelan et al. 1985; Banner 1990). All the directional model functions describe a narrow distribution near the spectral peak. Away from the peak, the spreading increases toward both higher and lower wave frequencies. The dependence on wave age among different model functions is considerably different. The strongest wave-age dependence is in the distribution of Mitsuyasu et al. (1975). A weak dependence is found in the function of Hasselmann et al. (1980). The distribution function of Donelan et al. (1985) and Banner (1990), on the other hand, is not dependent on the wave age. Young (1994), Hasselmann et al. (1980), and Donelan et al. (1985) have discussed whether the directional distribution should be a function of wave age, and they concluded that the answer depends on which physical process is controlling the characteristics of the directional spreading. If it is nonlinear wave–wave interaction, then wave age should play no role. If, however, wind input is the controlling factor, then directional distribution should be a function of wave age. Accurate determination of the directional distribution function thus serves as a diagnostic tool for the investigation of key mechanisms governing the dynamics of ocean waves.

More discussions on the directional distribution of a random wave field will be presented in Part II (Hwang et al. 2000). It suffices to say that there are significant disagreements in resolving directional distribution prop-

* U.S. Naval Research Laboratory Contribution Number JA/7332-99-0015.

+ Additional affiliation: NOAA/ETL, Boulder, Colorado.

Corresponding author address: Dr. Paul A. Hwang, Oceanography Division, Naval Research Laboratory, Stennis Space Center, MS 39529-5004.
E-mail: paul.hwang@nrlssc.navy.mil

erties based on measurements from a small number of sensor elements such as the pitch-and-roll buoys or wave gauge arrays. Depending on the chosen method in the analysis procedure, significant quantitative differences occur. The ideal database for the determination of the directional properties of random waves is the three-dimensional (3D) ocean surface topography. High-resolution directional distribution has been reported using an airborne stereo photographic technique (Cote et al. 1960; Phillips 1958), airborne radar system (Jackson et al. 1985), and land-based imaging radar (Wyatt 1995). Recently, an airborne topographic mapper (ATM: an airborne scanning laser ranging system) has been deployed for mapping surface waves. The ATM system completed three wave mapping missions at Duck, North Carolina, in 1994 and 1997. The datasets acquired cover a small yet interesting cross section of the environmental conditions. The first dataset (17 October 1994) represents a wind-generated sea on background swell. The second dataset (18 October 1994) is an ideal swell condition. The third dataset (24 September 1997) covers the conditions of quasi-steady and active wind generation (1200–1400 UTC) and decaying wind waves (1400–1600 UTC). The continuous spatial measurements cover tens of kilometers across the continental shelf, and offer a unique opportunity to study the wave dynamics and wave kinematics in a littoral region. For example, Hwang et al. (1998) present a spectral analysis of the swell case (18 October 1994) from the 3D ocean surface topography obtained by a scanning radar altimeter, which operates in a similar manner to that of the scanning laser altimeter. The dissipation rate of shoaling ocean swell is calculated from the spatial variation of the wavenumber spectra and the energy flux along the flight path. The results show that the lower bound of the measured dissipation rate is well defined by the analytical solution of bottom dissipation based on a quadratic shear stress formulation (Thornton and Guza 1983). Data points with dissipation rates well above the bottom dissipation prediction appear to be associated with noticeable bottom features and suggest that bathymetric scattering needs to be taken into consideration in the analysis of swell decay.

In this paper, the case of active wind wave generation (24 September 1997) will be analyzed. The environmental conditions of the field experiment are described in section 2. The measurement technique of the airborne scanning lidar and the data processing procedure are presented in section 3. The wavenumber spectral analysis is shown in section 4. A comparison of the ATM spectra with measurements from an offshore buoy is presented. Also, spectral slopes and dimensionless spectral coefficients are computed. The results are in excellent agreement with existing data. A summary is given in section 5.

The results from this study establish our confidence in the quality of the spatial data measured by the airborne scanning lidar system. The properties of the directional distribution functions are subsequently investigated. The results are given in Part II. Functional forms of a few key parameters of the distribution function (spreading factor and bimodal features in terms of the lobe angle and lobe ratio) are established from the spatial measurements.

2. The field experiment and environmental conditions

During the 1997 mission, the aircraft (a Twin Otter) flew 4 h (from 1200 to 1600 UTC) near Duck, North Carolina, on 24 September 1997. The slope of the bottom topography is mild at the experimental site. The water depth decreases gradually from 30 m at approximately 50 km offshore to 20 m at approximately 6 km offshore (Fig. 1). The aircraft flew a repeat race track pattern with two long legs perpendicular to the coastline (shown as solid line segments in the figure). The length of each long leg is approximately 40 km. The data presented here are from the inbound tracks. The orientations of the coastline, the flight direction, and the predominant wind direction are shown in the inset sketch in Fig. 1. In this paper, the coordinates are referenced to the flight track. The along-track direction is x_1 (positive toward beach) and the cross-track direction is x_2.

In situ wind and wave data are available from the suite of instruments maintained by the U.S. Army Field Research Facility (FRF) and a pitch-and-roll buoy (station ID 44014) maintained by the National Data Buoy Center (NDBC), National Oceanographic and Atmospheric Administration (NOAA). The locations of both stations are also shown in Fig. 1. As illustrated, the flight paths are between the two stations. The environmental data described in the following include information on wind, wave, and air and water temperatures. The wind speed and direction are extracted from the archive data of the weather station at the end of the FRF pier (600 m from shore) and the offshore buoy (ID 44014, at approximately 85 km offshore and 50-m depth). Wave height, wave period, and wave direction are obtained from the offshore buoy (ID 44014) and a nearshore waverider buoy (FRF instrument ID 630) located at 4 km from the beach. The air and water temperatures are from the offshore buoy (ID 44014). These environmental conditions are displayed in Fig. 2.

As shown by the wind record, a front passed through the area the night before the airborne mission. (Short line segments in Fig. 2 indicate the time of airborne data acquisition.) At the FRF site, wind speed (Fig. 2a) increased from 4 to 12 m s^{-1} within a 2-h period (0230–0430 UTC September 24) and wind direction shifted from westerly to northerly (Fig. 2b). Wind speed was quasi-steady at approximately 9.5 m s^{-1} from 0600 to 1300 UTC 24 September and then decreased from 9.5 m s^{-1} at 1300 to 5.5 m s^{-1} at 1600 UTC. The wind conditions at the offshore buoy site lag behind the FRF site by approximately 1.5 h. By the time of airborne

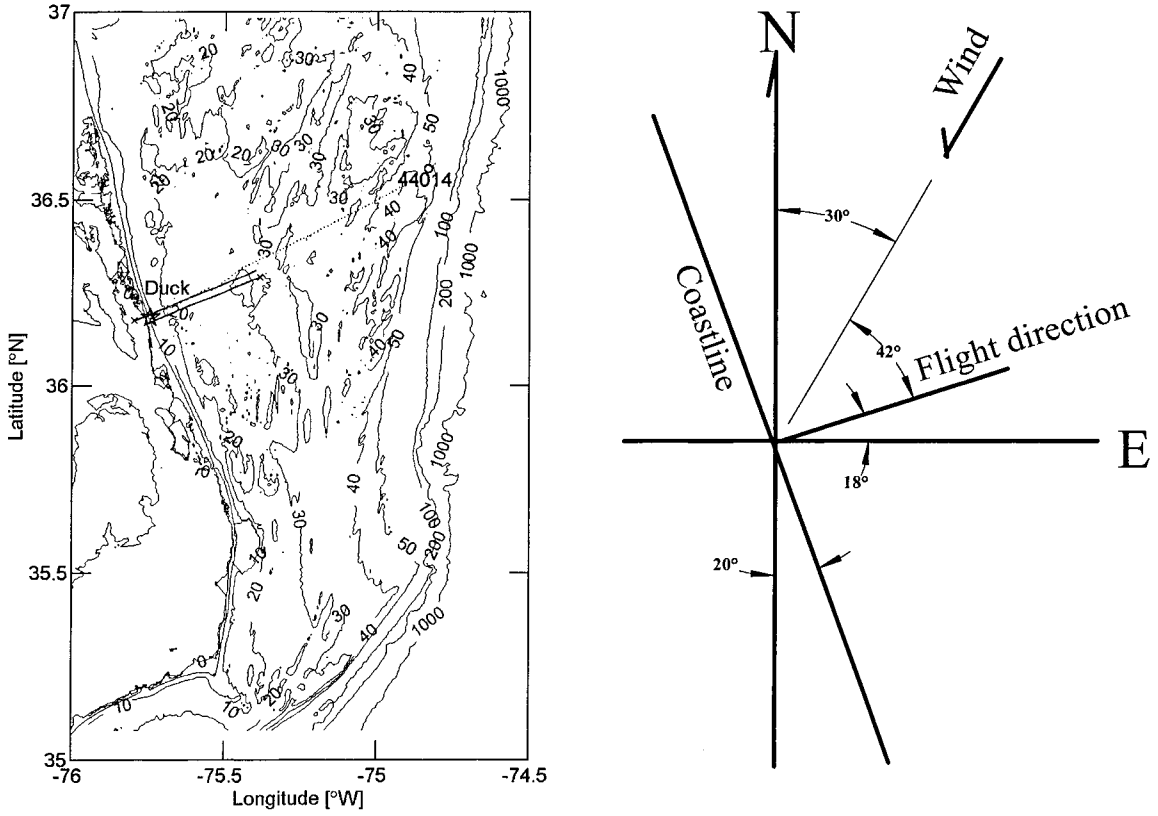

FIG. 1. The flight tracks superimposed on the coastline and bathymetry of the experimental site. The locations of NDBC buoy station 44014 and the U.S. Army Field Research Facility (Duck) are also shown. The sketch on the right illustrates the relevant orientations. The coordinate system for data processing is referenced to the flight direction (x_1 is along the flight direction, positive inshore).

measurements (1200 UTC), the wind conditions (speed and direction) at the two stations are almost identical, suggesting a homogenous wind field in the region. The spatial homogeneity of the wave field is confirmed by the ATM wave data and further discussion will be presented in the next section. Throughout the period of the frontal passage, the wind veered clockwise continuously. The rotation rate of the wind direction is relatively slow during the 4-h flight period and was quasi-steady at 30° from north (Fig. 2b).

The front generated a new wave system. At the FRF site, the significant wave height increased rapidly from 0.5 to 1.2 m within 2 h in response to the rapid increase in wind speed (Fig. 2c). The peak wave period also increased from 2.5 to 6 s during the frontal passage (Fig. 2d), and the dominant wave direction shifted from southeasterly to northerly (Fig. 2e). The wave field was dominated by a low gentle swell system coming from southeast in the region prior to the arrival of the front. Swell periods of approximately 8 s and wave heights of 0.6 m were recorded at both the nearshore and offshore buoy stations. The record from the nearshore buoy station suggests that the swell was decaying slowly in the shoreward region. There was a lag in the wave response to the wind change. The wave record shows that the significant wave heights and peak wave periods were quasi-steady during the first 2 h of flight (1200–1400 UTC). The wave conditions were typical of a decaying wave field for the last 2 h (1400–1600 UTC). Throughout the mission, the average flight track orientation (averaged over 20 segments for each flight track, and each segment covered a distance of approximately 1.5 km) was 18.3 ± 3.2° relative to east. The average flight speed was 64.3 ± 4.7 m s^{-1}. In the coordinate system referenced to the flight direction, the wind direction is 42° (Fig. 1, inset sketch).

Due to the frontal passage the air–sea stability condition was mildly unstable. The water temperature varied from 21.4°C at the beginning of the flight, dropped to 21.1°C at the middle, and went back up to 21.2°C at the end. The air temperature varied at a similar pace, from 19.9° to 19.1°C and then climbed back up to 19.7°C. The average stability condition represented by the bulk Richardson number is −0.007. The bulk Richardson number is computed from

$$\mathrm{Ri}_b = \frac{gz(T_a - T_w)}{U^2(273 - T_a)}, \tag{1}$$

where g is the gravitational acceleration, z is the in-

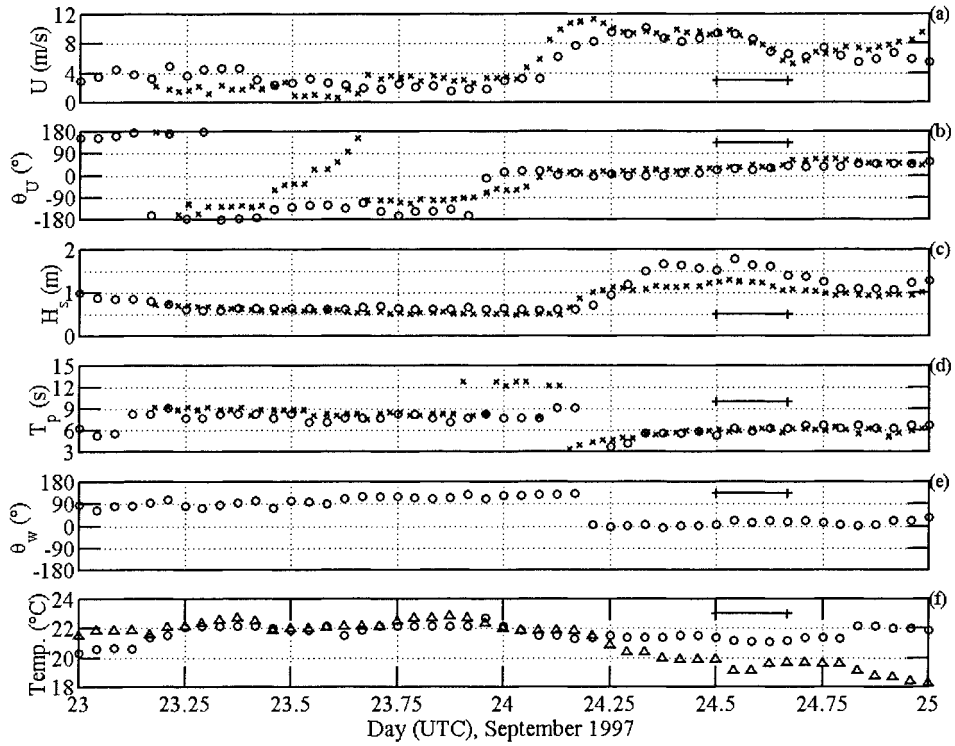

FIG. 2. The experimental conditions of (a) wind speed, (b) wind direction, (c) significant wave height, (d) peak wave period, (e) wave direction, and (f) air (triangles) and water (circles) temperatures, during the period of 23–25 Sep 1997. The short line segment in each panel represents the time of airborne wave measurements. Data from the offshore buoy (NDBC station ID 44014) are shown with circles or triangles, and data from FRF instruments are shown with crosses. Wind and wave directions in this figure are referenced to north with their magnitudes increasing clockwise.

strumentation height (5 m) for air temperature (T_a in °C) and wind speed (U) measurements, and T_w is water temperature in °C.

3. Measurement techniques and data handling

The ATM measures the distance between the aircraft and the surface of the ground or ocean. The aircraft altitude is typically 500 m and the flight speed is approximately 60 m s^{-1}. The dispersion angle of the laser beam is 1 mrad and the footprint of the laser spot on the ocean surface is 0.5 m. The swath of the image is 250 m. The scanning pattern repetition rate is 10 Hz and the data sample rate is 5000 Hz. The coarsest spacing between neighboring image pixels is 1.6 m in the cross-track direction and 6 m in the along-track direction. Detailed information on the ATM has been reported elsewhere (Krabill and Martin 1987; Krabill et al. 1995a,b; Hwang et al. 1998), additional information pertaining to the processing of the data used in this article is given here.

The ATM was originally designed to measure the height change in the Greenland Ice Cap (Krabill et al. 1995a,b). To minimize the dependence of return signals on the incidence angle, a circular scanning pattern was selected. In this scanning mode, the incident angle is maintained at a constant angle (15° in the present system). When applied to ocean wave measurements, the issue of time lag in the cross-track direction needs to be addressed. Also, to take advantage of the software developed for geophysical data analysis (e.g., 2D spectral analysis and image display), regridding of data into rectangular coordinates is essential. In the regridding process, duplication of data points in the new grid cells invariably occurs. Data duplication represents a waste of measurements since only one value can be kept in each cell in the final data product. The optimal selection of the grid size needs to be studied.

To investigate the data density and time lag issues, the locus of laser scanning is simulated for the conditions corresponding to the 1997 experiment. The airspeed is assumed to be 60 m s^{-1} and the radius of the major axis r of the locus is 125 m (corresponding to an aircraft altitude of 500 m for the 15° scanning angle, resulting in a 250-m swath). The scanning pattern repetition rate is 10 Hz and the data sample rate is 5000 Hz. A small segment (250 m × 250 m) of the laser trajectories is shown in Fig. 3a. It is obvious that the projection of a circular scanning pattern into rectangular

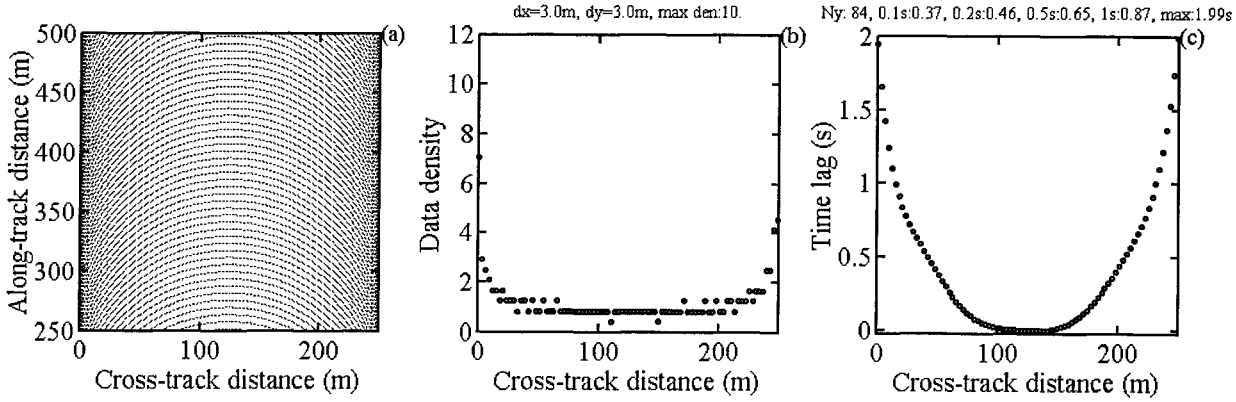

FIG. 3. (a) A simulated section of the scanning lidar trajectories on the ocean surface with the flight configurations corresponding approximately to those operated in the experiment. (b) The number of date points of the scanning measurements in each grid when resampled into rectangular coordinates. (c) The time lag (with respect to the central element) along a cross-track row.

grids does not yield an even distribution of data density in the new grids.

The optimal grid size (D_x in the along-track, and D_y in the cross-track directions) can be calculated from the flight speed, aircraft altitude, scanning angle, and sample rate. The along-track grid size D_x is calculated by the distance advanced by the aircraft over one period of scan cycle. Since the aircraft velocity is 60 m s^{-1} and the period of scan cycles is 0.1 s, this distance is 6 m. The cross-track grid size is determined by the arc length of the sampling spacing. This can be approximated by $2\pi r/500$, that is, approximating the oval trajectory by a circle of radius r and dividing the circumference by the sample rate of each cycle. With the given flight and data sampling configurations $D_{x_0} = 1.6$ m and $D_{y_0} = 6$ m are the optimal grid spacing. Computationally, square grids possess certain advantages. For example, the ranges of directional resolution and wavenumber resolution can be maintained symmetric in k_1 and k_2 directions. Such considerations become important in the analysis of the spectral directional properties to be discussed in Part 2. Following some experimentation with combinations of D_x ranging from 1.26 to 10 m and D_y ranging from 2 to 10 m, square grids of $D_x = 3$ m and $D_y = 3$ m were finally chosen (notice that $D_x \cdot D_y \approx D_{x_0} \cdot D_{y_0}$). No significant difference in the spectral properties in the wavenumber range $k \leq 0.5$ rad m^{-1} was found for the tested grid sizes. The cutoff wavenumber at 0.5 rad m^{-1} is determined by the fact that the coarsest spacing in the raw data is 6 m, which corresponds to the distance the aircraft advances in one scanning cycle (60 m $s^{-1} \times 0.1$ s). An example of using rectangular grids (1.26 m $\times$ 6 m) is presented in Hwang et al. (2000b).

The number of data points falling into each grid can be tallied. The results for $D_x = D_y = 3$ m are shown in Fig. 3b. Although the cross-track grid size (3 m) is almost two times the spacing in the raw data (1.6 m), the along-track cell size (3 m) is less than the coarsest distance between consecutive laser scans (6 m) and there are unfilled cells (data dropouts). In the central portion of the image, the dropout rate is almost 50% (i.e., every other cell contains approximately two raw data points but only one is retained). For the field data, additional dropouts occur at the two edges of the swath due to aircraft maneuvering to maintain course. An example of the topographic images from field measurements is shown in Fig. 4, illustrating typical meandering of the aircraft in motion. Further discussion of the wave properties revealed from these images will be presented later. The surface elevations in these blank cells are linearly interpolated from the neighboring cells. Several interpolation schemes were explored. One-dimensional interpolation in the along-track direction is found to produce the best result in terms of creating the least amount of discontinuous features on the surface topography. The variance of the interpolated topography was found to differ no more than 5% from that of the pre-interpolated topography. One drawback of this linear interpolation scheme is that it creates stripes along the two edges of the swath if the aircraft meander is substantial. A good example is shown in the image in Fig. 4b, the linear features in the upper middle side of the swath edge and the two end regions in the lower edge are produced by the interpolation procedure. These stripes appear as artificial ''wave trains'' and show up in the 2D wavenumber spectrum at $k \approx 0.5$ rad m^{-1} and $\theta \approx \pm 90°$. In the quantitative analysis of the directional distribution, this portion of the spectral data needs to be excluded.

Of more concern to the analysis of ocean waves is the relative time delay in the along-track and cross-track directions. For mapping of fixed objects such as an ice sheet, the time delay does not pose a problem. But in the case of ocean waves that propagate with a nonnegligible phase speed compared to the aircraft speed, the nonuniform cross-track time lags may introduce an error in the interpretation of the wave phase. The time lag in the along-track direction is due to relative motion of the aircraft and the propagating waves. This is a linear trans-

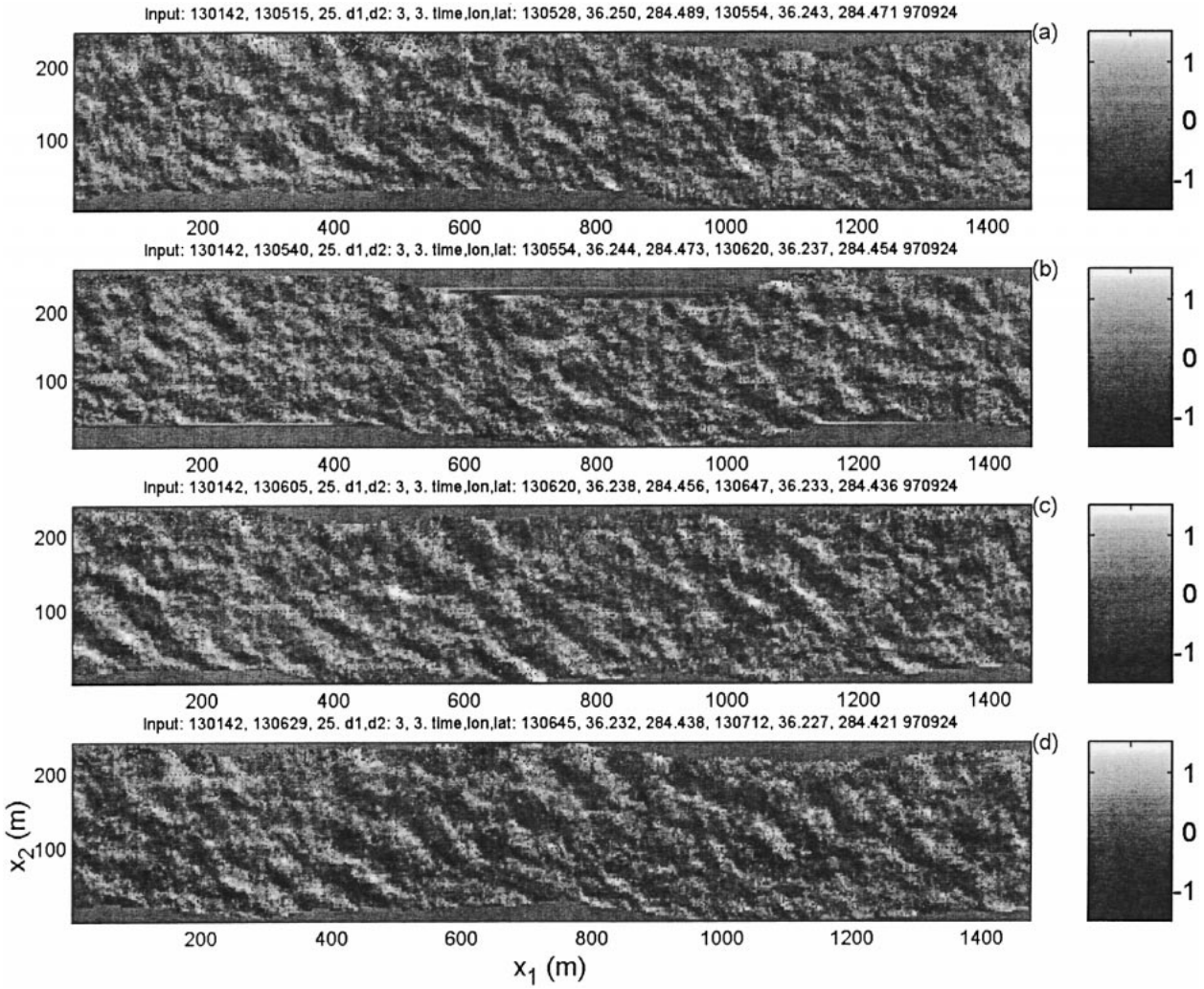

FIG. 4. Four consecutive images of the topography of ocean surface waves measured by the airborne scanning lidar system. The intensity level indicates the surface elevation (the unit of the grayscales is in meters).

lation issue (the familiar Doppler shifting of frequency or wavenumber) and will be discussed in the next section on wavenumber spectrum. The time lag in a cross-track row with respect to the central element is plotted in Fig. 3c. The data segment that is coherent to within 0.1 s is limited to the central 37% region. As the time lag allowance increases, the percentage of image within a given time lag also increases. With a 0.5-s lag the fraction is 65%, and for a 1 s lag it is 87%. The maximum time lag is 1.99 s at the two edges. For our purpose of resolving wave components longer than 12 m (the conservatively estimated Nyquist wavelength), the equivalence of approximately 1-Hz sample rate in the cross-track direction is sufficient. Higher precision can be achieved at the expense of discarding data near the two edges of the swath.

The vertical resolution of the ranging is dictated by the determination of the aircraft position. The theoretical resolution of the kinematic GPS system is 0.01–0.02 m. A dynamic calibration of the GPS measurements and the laser ranging of a calm water body shows that the rms error of the vertical resolution to be 0.08 m (Krabill and Martin 1987). The total error budget for an individual laser footprint location comprises 0.03 m (rms) for range, 0.05 m for GPS position, and 0.05 m for attitude-induced errors.

4. Wavenumber spectral analysis

a. Data processing procedure

Figure 4 shows a sequence of four consecutive images of the ocean surface topography obtained by the scanning lidar system. The coordinates of latitude/longitude in the original data have been rotated to the orthogonal coordinates referenced to the along- and cross-track directions, represented by x_1 and x_2 respectively. The image intensity is proportional to the wave elevation.

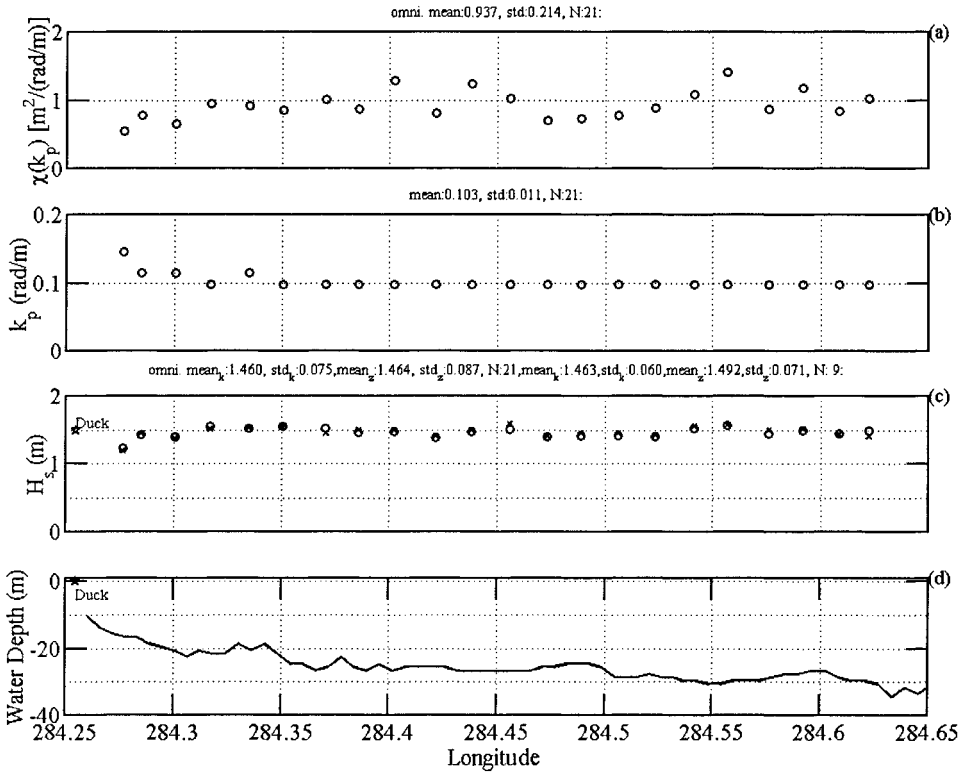

FIG. 5. Cross-shore distribution of (a) the peak spectral density, (b) peak wavenumber, (c) significant wave height, and (d) local water depth.

Grayscales for the range from −1.5 to 1.5 m are shown to the right of the images. The dominant direction of wave propagation is estimated to be approximately 45° (reference to the flight track) from examining these images. This is very close to the average wind direction, 42° relative to the flight direction as sketched in Fig. 1. There are also considerable 3D structures showing the short-crested nature of the wave field. A more quantitative analysis of the directional distribution is given in Part II. As discussed earlier (section 2), wind and wave data from two nearby buoy stations suggest that the environmental conditions during the experimental period are quasi-steady and quasi-homogeneous. The spatial homogeneity of the wave field is confirmed from the continuous spatial measurements by the airborne scanning lidar system. Figure 5 plots the cross-shore variation of the omnidirectional peak spectral density, peak wavenumber, and significant wave height. The integral properties of peak wavenumber and significant wave height show only minor fluctuations in the offshore region where water depth is more than 25 m and the wave condition is effective deep water. For reference, the local water depth along the flight track is plotted in Fig. 5d. More discussions on the omnidirectional wavenumber spectrum will be presented later.

Two-dimensional wavenumber spectra are calculated using a standard 2D FFT procedure. The results presented in this paper are processed using MATLAB. Each of the 2D spectra is calculated from an image of 128 × 128 pixels of 3 m × 3 m. Because the width of the 2D FFT image is wider than the lidar swath (approximately 250 m), zeros are filled in the area without data. The spectral energy is adjusted by the fraction of zero filling as a standard practice in spectral analysis (e.g., Bendat and Piersol 1971). Because the measurement was performed on a moving platform, the spectrum calculated is in terms of the encounter wavenumber, which is different from the true wavenumber due to the effect of Doppler shifting (Walsh et al. 1985, 1989). The wavenumber is then corrected to the true wavenumber with the input of aircraft velocity and local water depth. This procedure is applied to all the wavenumber elements in the 2D wavenumber space. The magnitudes of the corrected wavenumber (k), propagation direction (θ), wave frequency (ω), and wave phase speed (c)—the last two quantities are calculated from the linear dispersion relation—of each element in the (k_1, k_2) space can all be calculated, where k_1 and k_2 are the wavenumber components in the along-track and cross-track directions. The 2D wavenumber spectrum can then be mapped into either (k_1, k_2), (k, θ), or (ω, θ) coordinates.

Smoothing is performed for each spectral element by averaging over a 3 × 3 m^2 region centered at the element. The weightings of 1, 1/2, and 1/4 respectively are applied for the central element, each of the four side elements, and each of the four corner elements. The

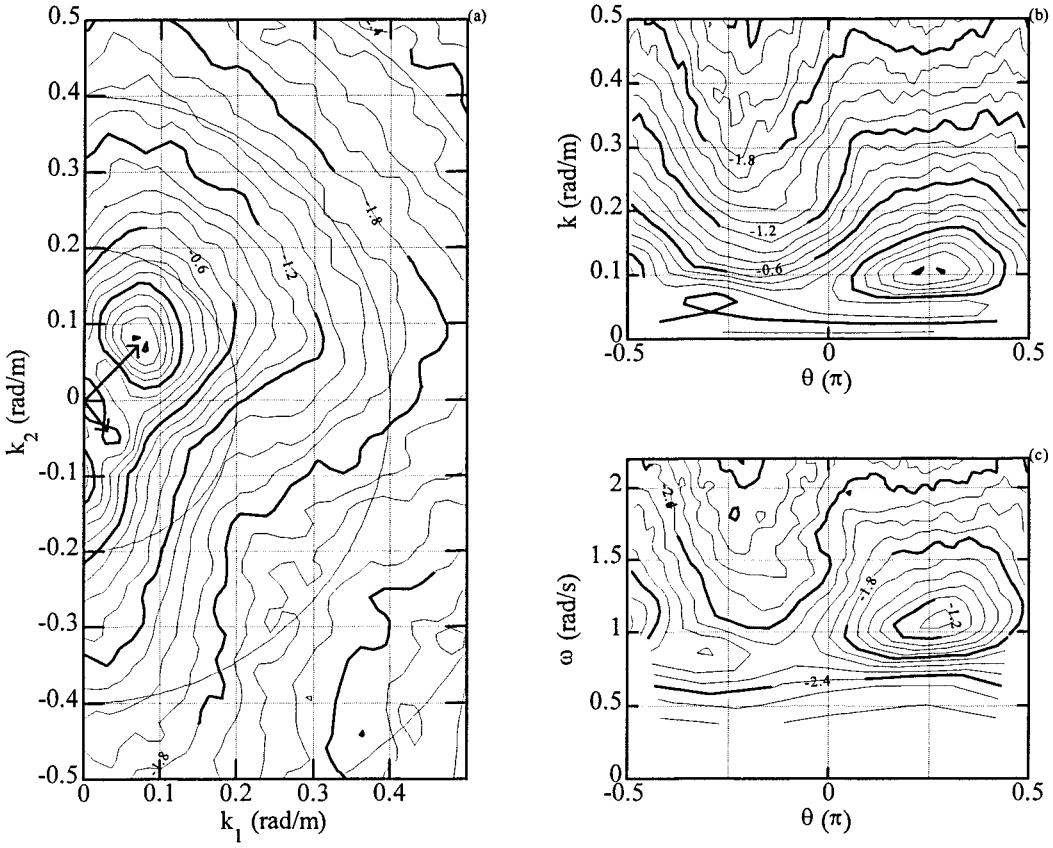

FIG. 6. Examples of the computed 2D wavenumber spectra. (a) Contour plot in (k_1, k_2) representation (same as polar representation). Wavenumber vectors for the dominant wind wave and the swell components are indicated by arrows. (b) Contour plot in rectangular (k, θ) representation. (c) Contour plot in rectangular (ω, θ) representation. Semicircles in (a) correspond to $k = 0.2$, 0.4, and 0.6 rad m^{-1}. The intervals are 6 dB apart (i.e., 0.6 in logarithmic scale) for the thick contours, and 1.5 dB apart for the thin contours.

effective degree of freedom (DOF) for the smoothed spectrum is 8, instead of 18 if weighting of unity is used for all elements in the averaging cells. Each ~1.5 km image (Fig. 4) produces three spectra, which are ensemble averaged. The DOF of the final 2D spectrum from each image is 24. A 2D white noise spectrum with a spectral density of 1.6×10^{-3} [m^2/(rad m^{-1})] over the resolved wavenumber range of $[-1, 1]$ rad m^{-1} in k_1 and k_2 (corresponding to 0.08 m total rms error discussed earlier) is subtracted from the 2D spectrum of each image.

The flight period is divided into two halves. As mentioned in section 2, the waves of the first half (2 hours) were quasi-steady. In the second half the waves were decaying. Thirty-six images (9 each from four tracks) from the offshore region are averaged for each half-period. This produced two 2D spectra, one for the quasi-steady case and the other for the decaying wave field. Each represents the average of 2 hours of data over an area of ~14 km × 0.25 km. The DOF of the spectra is 864.

b. General features of the wavenumber spectrum

An example of the resulting 2D wavenumber spectrum is shown in Fig. 6, presented as $\Psi(k_1, k_2)$ in (a), $\Psi(k, \theta)$ in (b), and $\Psi(\omega, \theta)$ in (c). In all the three plots, the thick contours are 0.6 apart (in logarithmic scale), and the thin contours are 0.15 apart (in logarithmic scale). The prominent features of these 2D spectra include (i) the peak of the spectrum is at $\theta_p \approx 45°$ and $k_p \approx 0.10$ rad m^{-1} (k_p is determined from the results of omnidirectional spectral analysis as shown in Fig. 5 and to be further discussed later). The dominant wave direction is within 5° of the average wind direction (Fig. 1). (ii) A weak swell component can be identified at $k \approx 0.05$ rad m^{-1} and $\theta \approx -50°$. The wavenumber vectors of the dominant wind wave and the swell components are indicated by arrows in Fig. 6a. (iii) The directional distribution is generally symmetric with respect to the dominant wave direction. The spreading becomes broader as wavenumber increases and shows multimodal structure, of which a bimodal feature is most distinct. Bimodal distribution starts to develop for wave-

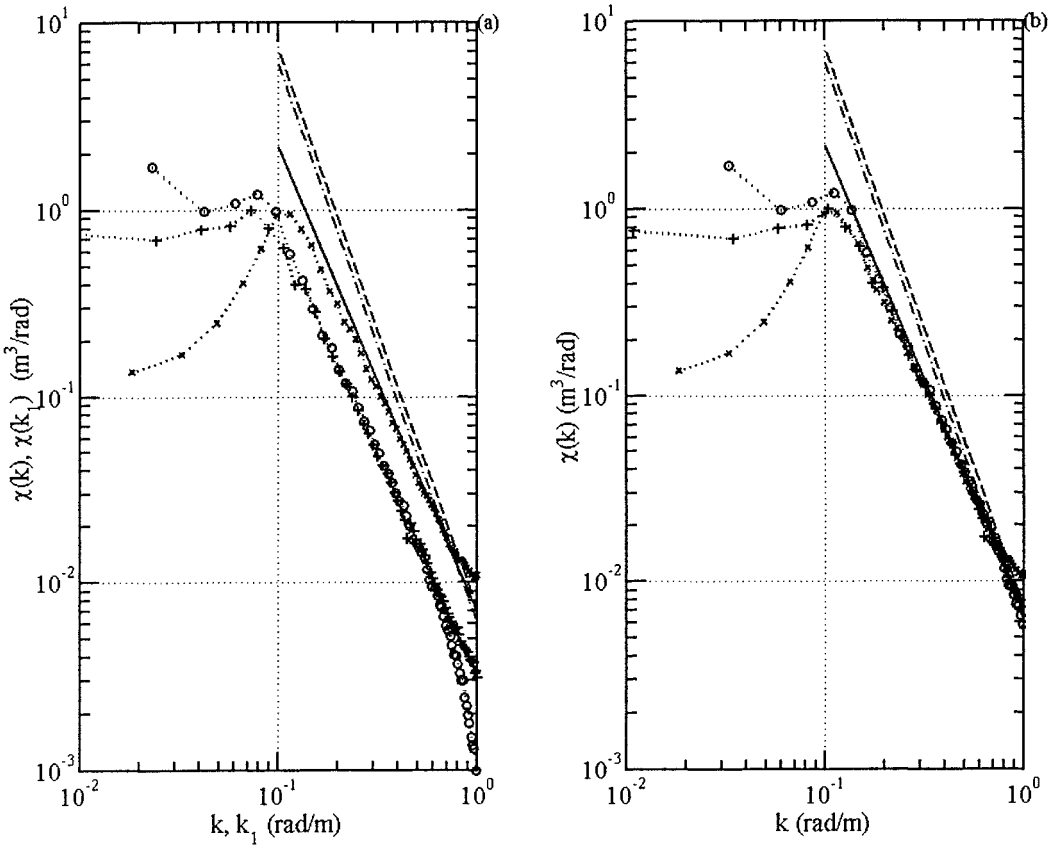

FIG. 7. (a) A comparison of three 1D wavenumber spectra. Crosses: omnidirectional spectrum, pluses: marginal spectrum in the flight direction, circles: traverse spectrum in the flight direction, solid curves: $\chi(k) = 0.06u_*g^{-0.5}k^{-2.5}$ (Phillips 1985), dashed–dotted curves: $\chi(k) = 0.006k^{-3}$ (Phillips 1977), and dashed curves: $\chi(k) = 0.002(u_*/c)(c_m/c)k_mk^{-4}$ (Hwang et al. 1996; Hwang 1997). (b) Same as (a) but the transect wavenumber is adjusted by the projection equation (4).

numbers slightly greater than $\sim 2k_p$ ($1.4\omega_p$). Angular separations of the distribution lobes increase toward higher wavenumber or wave frequency. More quantitative analysis of the directional distribution will be presented in Part II.

c. One-dimensional wavenumber spectra

From the 2D spectrum, two different one-dimensional (1D) spectra are computed. The first is the omnidirectional spectrum calculated by

$$\chi(k) = 2\int_{-\pi/2}^{\pi/2} \Psi(k, \theta)k\, d\theta. \tag{2}$$

The second is the marginal spectrum integrated over k_2,

$$\chi(k_1) = 2\int_{-k_{2\max}}^{k_{2\max}} \Psi(k_1, k_2)\, dk_2, \tag{3}$$

where $k_{2\max}$ is the Nyquist wavenumber of k_2. Similarly, the marginal spectrum integrated over k_1 can be derived from the 2D spectrum. The factor of 2 in the above equations accounts for the fact that only one half-plane of the 2D spectrum is used because of the 180° ambiguity inherent in the 2D spectrum derived from a stationary image, and the correction procedure applied to convert the encounter wavenumber to true wavenumber. One-dimensional (traverse) spectra can also be computed from image transects along any orientation of the 3D surface topography. In particular, if the traverse direction is in the along-track or cross-track direction, the resulting 1D spectrum is identical to $\chi(k_1)$ or $\chi(k_2)$, respectively.

Another 1D spectral representation is the transect of the 2D spectrum for a given propagation angle θ_*, that is, the spectral transect, $\Psi(k, \theta_*)$. From inspecting Fig. 6, it is clear that there is no simple expression for $\Psi(k, \theta_*)$ and a full description of the directional distribution is needed (Part II). In this section we shall only discuss the omnidirectional spectrum, $\chi(k)$, and the marginal or traverse spectrum in the flight direction $\chi(k_1)$. [Both marginal and traverse spectra are expressed as $\chi(k_1)$ since theoretically they are the same property but computed by two different methods.] Figure 7a shows

a comparison of the three 1D spectra. The spectral slope is very close to -2.5 in the higher wavenumber end of the spectra. For reference, the spectral functions of $\chi(k) = 0.06u_* g^{-0.5}k^{-2.5}$ (Phillips 1985), $0.006k^{-3}$ (Phillips 1977), and $0.002(u_*/c)(c_m/c)k_m k^{-4}$, which becomes $0.002u_* c_m k_m g^{-1}k^{-3}$ in the gravity range (Hwang et al. 1996; Hwang 1997), are plotted as solid, dashed–dotted, and dashed curves in the figure. As expected, the traverse spectrum (circles) and the marginal spectrum (pluses) are similar. Compared to the omnidirectional spectrum (crosses), the traverse and marginal spectra overestimate the spectral density in the long-wave portion, and underestimate the spectral density in the shorter wave components. The spectral peak is obviously downshifted. This is mainly due to the projection of wavenumber into the flight direction. The effect would have been minimized if the flight track were along the dominant wave direction, θ_p. In the present configuration, the flight track is approximately 45° oblique to the dominant wave propagation. Applying the relation

$$k_1 = k\cos\theta_p, \tag{4}$$

the three 1D spectra are replotted in Fig. 7b. The agreement improves significantly. It is quite surprising that the traverse spectrum can be ''adjusted'' to agree with the omnidirectional spectrum through a simple projection of the wavenumber into the flight direction by Eq. (4). Whether this is a fortuitous coincidence for this particular wind and wave condition remains to be determined after a sufficient number of datasets with different environmental conditions are available.

During the whole flight mission, the peak wavenumbers of the wave spectra in the offshore locations remain close to 0.10 rad m^{-1} based on the analysis of the omnidirectional spectra (Fig. 5b). This peak wavenumber is slightly lower than the expected peak wavenumber of a wind-generated wave field with $C_p/U_{10} = 1$, for which k_p can be calculated by

$$k_{p,1} = \frac{g}{U_{10}^2}, \tag{5}$$

where U_{10} is the neutral reference wind speed at 10-m elevation and C_p is the phase velocity of the wave component at the spectral peak. For the quasi-steady period in the present experiment, $U_{10} \approx 9.5$ m s^{-1}, and $k_{p,1} = 0.11$ rad m^{-1}. The measured peak wavenumber is about 1.3 times higher than the peak wavenumber of a fully developed wave field for the given wind speed (Pierson and Moskowitz 1964)

$$k_{\mathrm{FD}} = \frac{g}{(1.2U_{10})^2}. \tag{6}$$

With the substitution of $U_{10} \approx 9.5$ m s^{-1}, $k_{\mathrm{FD}} = 0.075$ rad m^{-1}. At the experimental site, the fetch for a north to northeasterly wind is essentially unlimited. The wave field reported here is duration-limited.

d. Comparison with buoy measurements

Figure 8 compares the omnidirectional wavenumber spectra measured by the airborne scanning lidar with those obtained from the offshore buoy (NDBC buoy ID 44014). Twenty minutes of wave data at the buoy station were acquired every hour (from the 20th to the 40th minute) and reported at the beginning of the following hour. Hence, buoy wave data at 1300 and 1400 UTC are averaged and compared to the first 2 hours of the ATM data. Similarly, buoy wave data at 1500 and 1600 UTC are averaged and compared to the last 2 hours of the ATM data. The DOF of the buoy spectra is 66. The average spectra for the first two hours of flight time are shown in Fig. 8a, and those for the last two hours of flight time are shown in Fig. 8b. The relation between the 1D frequency and wavenumber spectra is

$$\chi(k) = \chi(\omega)\frac{d\omega}{dk}$$

(e.g., Phillips 1985). The frequency range of the NDBC frequency spectra is from 0.03 to 0.4 Hz, corresponding to the wavenumber range of 3.6×10^{-3} to 6.4×10^{-1} rad m^{-1}. The spectral peak frequency is 0.16 Hz, corresponding to 0.10 rad m^{-1}, in excellent agreement with the ATM result. In this figure, the full range of the wavenumber derived from the ATM data are displayed. The Nyquist wavenumber (0.5 rad m^{-1}) conservatively determined by the coarsest spacing in the raw dataset (6 m) is marked with a dashed curve in each plot.

The spectral slopes in the high wavenumber regions are very close to -2.5 for both ATM and buoy spectra. The solid curves plotted in the figures correspond to $\chi(k) = 0.06u_* g^{-0.5}k^{-2.5}$. The spectral density of the buoy data is generally higher than that of the ATM measurements. The significant wave heights of the airborne lidar measurements (1.46 and 1.35 m for Figs. 8a and 8b, respectively) are between those measured by the offshore buoy (1.73 and 1.46, respectively) and the nearshore buoy (1.27 and 1.17 m, respectively). With this consideration of the cross-shore variation of significant wave heights, the spectral comparison shown in Fig. 8 is determined to be very good. Note that the degrees of freedom of the ATM and the buoy spectra are significantly different (864 vs 72) and contribute to the observed differences of spectral densities at individual frequencies. Additional analysis of the buoy data and comparisons with airborne scanning lidar results are given in Part II and Wang and Hwang (1999, manuscript submitted to *J. Phys. Oceanogr.*).

e. The spectral slope and dimensionless spectral coefficient

Many papers have been published on the subject of spectral slope and spectral coefficient of ocean waves. Phillips (1985) presents a comprehensive review on the spectral and statistical properties of the equilibrium

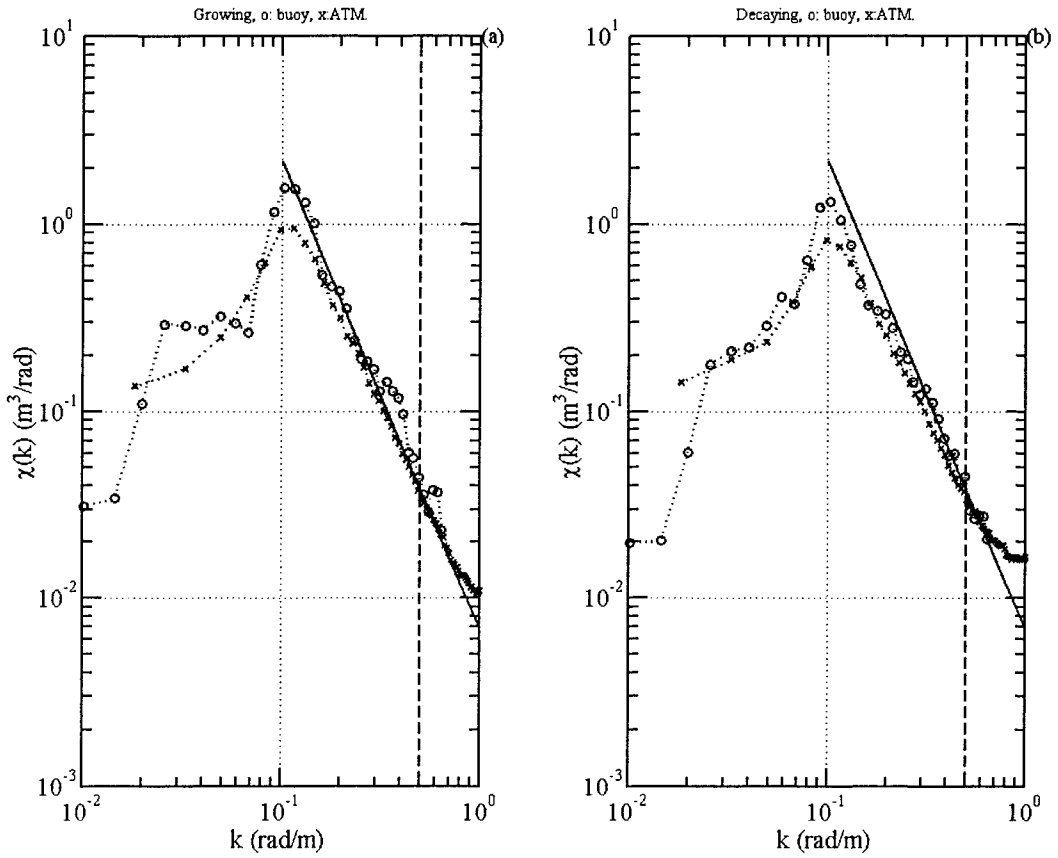

FIG. 8. A comparison of the omnidirectional spectra measured by ATM (crosses) and offshore buoy (ID 44014) (circles). (a) Average of the first 2 hours of data—quasi-steady condition, and (b) average of the last 2 hours of data—decaying wave field. Solid curves: $\chi(k) = 0.06u_* g^{-0.5}k^{-2.5}$ (Phillips 1985).

range in wind-generated waves. Extensive discussions are given for both wavenumber and frequency spectra. Through a detailed analysis, he reaches the conclusion that in the equilibrium range the 2D spectral density, $\Psi(\mathbf{k})$, of gravity waves increases linearly with wind friction velocity, u_*, and the spectral slope is -3.5. This can be expressed as $\Psi(\mathbf{k}) \sim u_* k^{-3.5}$ or, equivalently, for the 1D spectrum, $\chi(k) \sim u_* k^{-2.5}$. More precisely, the omnidirectional and the traverse spectra are

$$\chi(k) = 2\beta u_* I(p) g^{-0.5} k^{-2.5}, \quad \text{and} \tag{7}$$

$$\chi(k_1) = 2\beta u_* I(p + 3/2) g^{-0.5} k_1^{-2.5}. \tag{8}$$

In both equations, β is the dimensionless spectral coefficient, p is the exponent of the directional distribution represented by $\cos^p\theta$, and $I(x) = \int_{-\pi/2}^{\pi/2} \cos^x\theta \, d\theta$. In the past, the major data sources for the study of ocean wave spectral properties are frequency spectra from point measurements. A limited number of spatial measurements include wave gauge array data (e.g., Donelan et al. 1985) and stereo photographic measurements (e.g., Cote et al. 1960) were also used. Here we investigate the spectral slope and dimensional coefficient obtained from wavenumber spectra of the ocean surface topography obtained by airborne scanning lidar ranging.

1) DIMENSIONLESS SPECTRAL COEFFICIENTS IN THE EQUILIBRIUM RANGE

The dimensionless spectral coefficient β can be calculated from the measured wavenumber spectra using (7) or (8). Due to the limitation of wavenumber resolution in the ATM dataset, the range of $0.2 \le k \le 0.5$ rad m^{-1} (2–5k_p, or equivalently 1.4–2.2ω_p) is selected as approximately within the equilibrium range. As illustrated in Fig. 6 and to be further discussed in Part II, the directional distribution displays multiple lobes as wavenumber increases and obviously deviates from the simple $\cos^p\theta$ functional form. Equations (7) and (8) remain valid, however, for a more general directional distribution function $D(k, \theta)$, if the integration function is redefined as $I(q) = \int_{-\pi/2}^{\pi/2} D(k, \theta) \, d\theta$. For the discussion here, the functional form of the directional distribution $D(k, \theta)$ will not be specified, thus the quantity $\beta I(q)$ instead of β is investigated. In this fashion, the directional distribution is absorbed into the spectral coefficient βI, which can be calculated directly from the measured wavenumber spectra using (7) or (8).

The calculated spectral coefficients display a trend of slight increase with wavenumber (Fig. 9, plotting the results in both logarithmic and linear scales). The trend

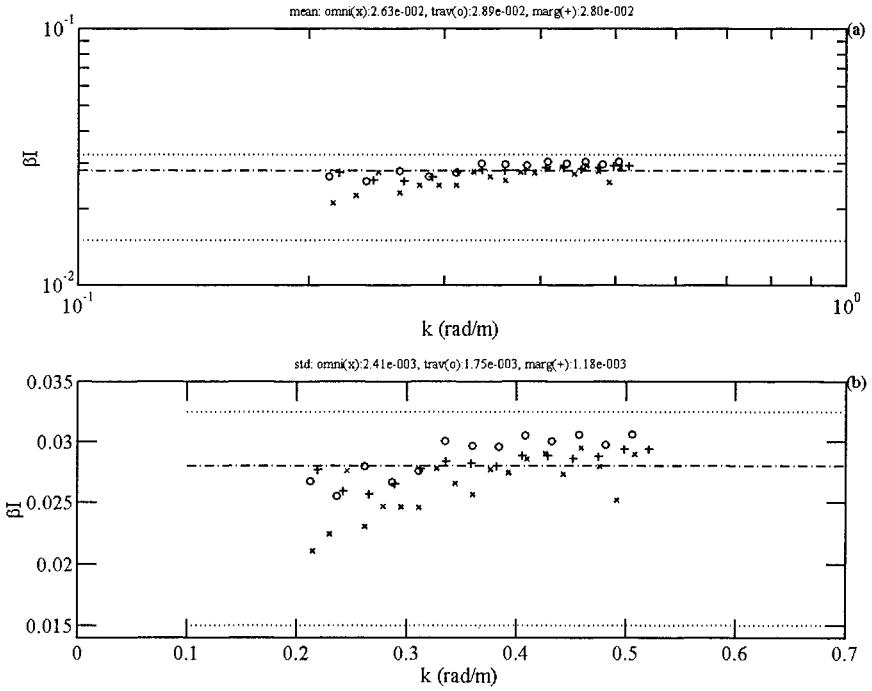

FIG. 9. Dimensionless wavenumber spectral coefficient βI (Phillips 1985) plotted in logarithmic scales (a) and linear scales (b). Crosses: omnidirectional spectrum, pluses: marginal spectrum, circles: traverse spectrum. The dotted curves correspond to $\chi(k) = 2\beta I u_* g^{-0.5} k^{-2.5}$, where $\beta I = 0.015$ and 0.03 and represent the range of reported field data based on frequency spectral analyses, the dotted-and-dashed curve is the average based on wavenumber spectral analyses from the ATM data discussed in this paper. Quasi-steady wave field.

reflects the difference in the measured spectral slopes with the slope of the spectral model given in (7) and (8). The average βI for the quasi-steady wave field (the first 2 h of data) is 2.63 ($\pm$0.24) $\times$ 10^{-2} from omnidirectional spectra, 2.80 ($\pm$0.12) $\times$ 10^{-2} from marginal spectra, and 2.89 ($\pm$0.18) $\times$ 10^{-2} from traverse spectra. For the decaying wave field (the last 2 hours of data), the average βI is 2.29 ($\pm$0.29) $\times$ 10^{-2} from omnidirectional spectra, 2.91 ($\pm$0.33) $\times$ 10^{-2} from marginal spectra, and 2.71 ($\pm$0.29) $\times$ 10^{-2} from traverse spectra (Fig. 10). Interestingly, based on the omnidirectional spectral estimate, the βI value in the decaying field is always less that that in the quasi-steady wave field across the wavenumber range of 2–5 k_p. In contrast, based on either marginal or transect spectral estimates, βI is in fact higher in the region $5 > k/k_p > 4$. Toba et al. (1988) present analysis of the response of wind wave frequency spectra to changing winds using field data collected from two locations, a tower located at the mouth of Tanabe Bay in southern Japan, and an oil platform in Bass Strait, Australia. Both datasets show a significant time lag between the time series of the dimensionless frequency spectral coefficient and the wind friction velocity. The spectral coefficient is inversely correlated to the variation of wind friction velocity with a timescale smaller than 20 min [see also discussions in Young (1999, section 6.3)]. The difference in the relaxation time or length scale observed from the omnidirectional spectral analysis and the results from frequency or transect wavenumber spectral analysis requires further investigation.

The numerical values of βI obtained from the ATM measurements are in excellent agreement with the numbers reported in the literature. For example, the analysis of Phillips (1985, p. 526) yields $\beta I = \alpha/4$, where α is Toba's coefficient for the frequency spectral function (Toba 1973). The α value is between 0.11 and 0.12 based on the present analysis of the wavenumber spectra. Phillips (1985, Table 1) summarizes results of α computed from frequency spectra obtained in the ocean environment. The observed values of α range from 0.06 (Kondo et al. 1973; Kawai et al. 1977; Mitsuyasu et al. 1980; Toba et al. 1988) to 0.11 (Kahma 1981; Forristall 1981). Battjes et al. (1987) reanalyze the JONSWAP data, which yielded a mean α value of 0.13. They also process the spectra reported in Donelan et al. (1985), the average α value of that dataset is 0.11. The upper and lower ranges of βI, 0.0325 and 0.015, obtained from the frequency spectral analyses are shown as dotted curves in Figs. 9 and 10. The dashed-and-dotted curve represent the mean value (2.8×10^{-2}) obtained from the wavenumber spectra in a quasi-steady wave field.

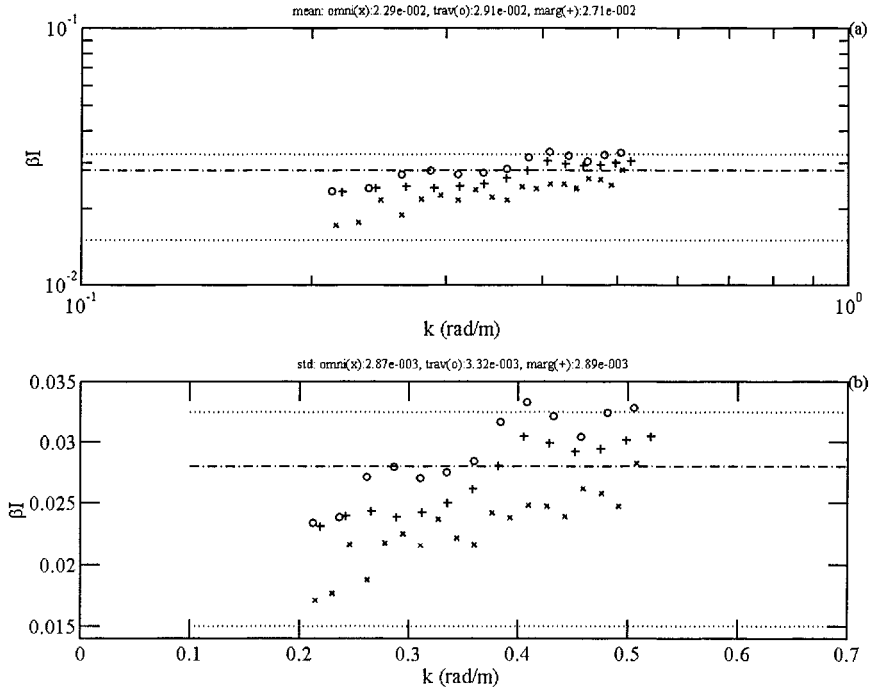

FIG. 10. As in Fig. 9 but for the decaying wave field.

2) SPECTRAL SLOPES

The slope of the measured wavenumber spectrum is less steep than -2.5 (Figs. 7 to 10). The spectral slope is determined by least square fitting the spectral densities in the wavelength range from $0.2 \leq k \leq 0.5$ rad m^{-1}. For the quasi-steady wave field, the average slope is -2.27 (± 0.042) based on the omnidirectional spectra, -2.40 (± 0.044) for the marginal spectra, and -2.28 (± 0.053) for the traverse spectra. For the decaying wave field, the average slope is -2.17 (± 0.087) based on the omnidirectional spectra, -2.3 (± 0.12) for the marginal spectra, and -2.27 (± 0.14) for the traverse spectra. The milder slope in the decaying wave field is due to the fact that as wind slackens, the primary region of wave dissipation is close to the spectral peak, as revealed from the temporal variation of the wavenumber spectrum (to be further discussed in the next section).

The milder (than -2.5) slope is due to the close proximity to the spectral peak. Indeed, in the frequency range 1.4 to $2.2\omega_p$, (corresponding to 2 to $5k_p$), the slopes of the frequency spectra reported in Donelan et al. (1985, Fig. 12) range from -3 to -3.5, rather than -4 that fits the higher frequency portion. As shown in Figs. 7, 9, and 10, if the range $0.3 < k < 0.5$ rad m^{-1} were used for the least square fitting, the slope would have been much closer to -2.5. Also, as discussed in section 4d, excellent agreement is found in the comparison of ATM spectra with measurements from an offshore buoy. The spectral slope obtained from the scanning lidar system is considered to be in excellent agreement with those obtained from frequency spectral analyses.

Banner (1990) has explained the reason for the slope difference between the omnidirectional and the traverse spectra. He considers the effect of wavenumber-dependent directional distributions on the slope of the traverse or marginal spectrum. The result shows that the spectral slope of the traverse spectrum is -3 for a 2D spectrum with an omnidirection spectrum of -2.5 slope and a wavenumber-dependent directional distribution revised from the sech squared [$\text{sech}^2(b\theta)$] function suggested by Donelan et al. (1985). The analysis can be generalized to show that the slope of the marginal or traverse spectrum in the along-wind direction is steeper than that of the omnidirectional spectrum if the directional distribution becomes broader with increasing wavenumber. The measured slope difference among the three 1D spectra within the resolved wavenumber range is qualitatively consistent with Banner's (1990) analysis although the quantitative difference in the traverse and omnidirectional spectral slopes is considerably much less than predicted. As shown in Fig. 6 and to be further discussed in Part II, the measured special directional distributions analyzed from the 3D surface wave topography are significantly different from the model function used in his computations.

f. Temporal evolution of wavenumber spectrum

The repeat race track operation provides seven consecutive visits to a given ocean surface area. This temporal sequence of data allows a rough estimation of the relaxation rate of the wave system. The energy balance

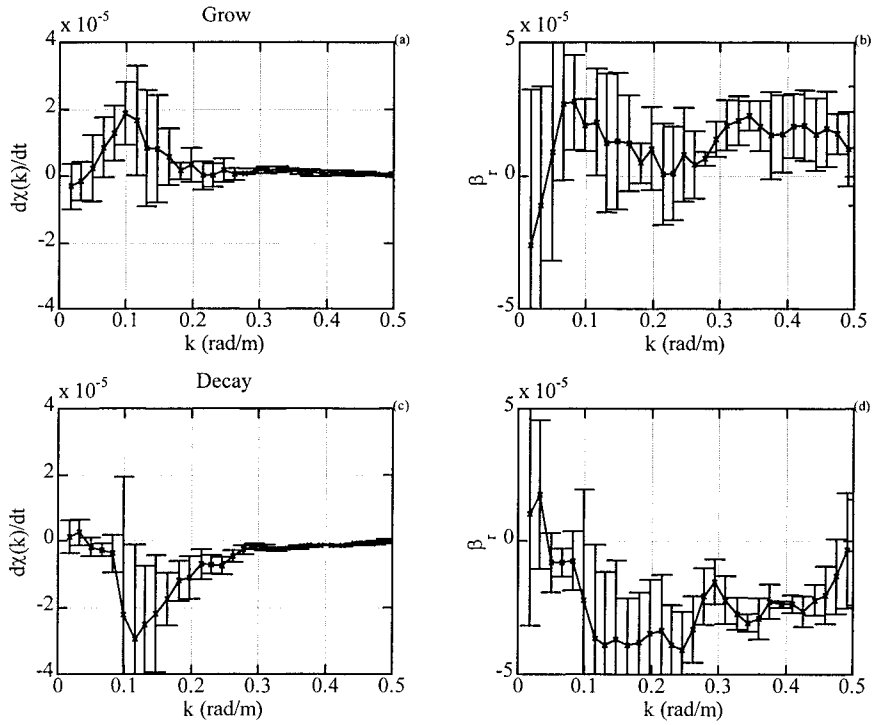

FIG. 11. The rate of change of the wavenumber spectral density (a, c) and the relaxation rate of the wave system (b, d). Panels (a) and (b) are for a quasi-steady wave field and (c) and (d) are for a decaying wave field. The error bars represent one standard deviation.

governing the dynamics of wave propagation can be expressed by the spectral energy conservation equation

$$\frac{\partial \chi(k)}{\partial t} + \nabla(\chi(k)\mathbf{C}_g(k)) = \sum Q_i, \tag{10}$$

where t is time, $\mathbf{C}_g$ is wave group velocity vector, and Q_i are the various source and sink terms. The most important source and sink functions are wind generation, wave breaking and wave/bed friction dissipation, and nonlinear wave–wave interaction. Expressing the right-hand side with a relaxation parameter,

$$\sum Q_i = \beta_r \chi(k), \tag{11}$$

Eq. (10) can be rewritten as

$$\frac{d\chi(k)}{dt} = \beta_r \chi(k). \tag{12}$$

As stated earlier, the wave field was observed to be quasi-homogenous. Therefore we combine nine image segments from each track, resulting in an average of spectral measurements from an area of 14 km × 0.25 km. The average time intervals among the seven consecutive visits is 0.56 h. The spectra from the first four tracks represent the wave properties in a quasi-steady wave field, and those of the last four tracks (the middle track is an overlap) represent the decaying wave field. As a first order approximation of the rate of change of the spectral density, $d\chi(k)/dt$, and the relaxation rate, $\beta_r = [d\chi(k)/dt]/\chi(k)$, can be estimated from finite difference of the time sequence of the wavenumber spectra. The results are presented in Fig. 11. For the quasi-steady wave field (Figs. 11a,b), the wave growth occurs primarily near the spectral peak. The relaxation rate is predominantly positive in the wavenumber range $0.05 < k < 0.5$ rad m^{-1}. For the decaying wave field (Figs. 11c,d), the wave decay occurs also near the spectral peak, the location of maximal decay is slightly higher than the spectral peak. The relaxation rate is predominantly negative in the wavenumber range $0.05 < k < 0.5$ rad m^{-1}.

5. Summary

An airborne scanning lidar acquires high-resolution spatial measurements of the topography of ocean surface waves. From these spatial data, 2D wavenumber spectra can be calculated in a straightforward fashion. We have presented an analysis of the field data collected from a recent experiment. The environmental conditions include both quasi-steady active wind wave generation and decaying wave field. Similarities and differences of three expressions of 1D wavenumber spectra are discussed (section 4). The wavenumber spectra obtained from the airborne scanning lidar are in excellent agreement with the output from an offshore buoy. Using the portion of the wavenumber spectral densities in the

range 2–5 times the spectral peak, the spectral slope and the dimensionless spectral coefficients (βI) in the equilibrium range are calculated from the wavenumber spectra. The results derived from the ATM-measured wavenumber spectra are found to be in excellent agreement with those obtained from frequency spectral analyses (Fig. 9). The study performed here establishes our confidence on the ocean surface topography measured by the airborne scanning lidar. The airborne operation provides efficient spatial measurements of the wave field. This is especially useful for the investigation of the spatial and temporal evolution of shoaling waves in the littoral zone. The 3D topography is also the ideal dataset for the quantitative determination of the spectral directional properties. The directional distributions of wind-generated surface waves are presented in Part II.

Acknowledgments. This work is sponsored by the Office of Naval Research through Naval Research Laboratory's research project ''Phase-resolved nonlinear transformation of shoaling waves'' (Program Element 62435N) and NASA's Mission to Planet Earth. We express our appreciation to the flight crew, the engineers, and technicians who successfully executed the field experiment and performed post processing of the ATM data necessary for the construction of the 3D surface topography. The in situ wind and wave data were supplied by the Field Research Facility, U.S. Army Corps of Engineers, and the National Data Buoy Center, NOAA.

REFERENCES

Banner, M. L., 1990: Equilibrium spectra of wind waves. *J. Phys. Oceanogr.*, **20,** 966–984.

——, and I. R. Young, 1994: Modeling spectral dissipation in the evolution of wind waves. Part I: Assessment of existing model performance. *J. Phys. Oceanogr.*, **24,** 1550–1571.

Battjes, J. A., T. J. Zitman, and L. H. Holthuijsen, 1987: A reanalysis of the spectra observed in JONSWAP. *J. Phys. Oceanogr.*, **17,** 1288–1295.

Bendat, J. S., and A. G. Piersol, 1971: *Random Data: Analysis and Measurement Procedures.* Wiley and Sons, 407 pp.

Cote, L. J., and Coauthors, 1960: The directional spectrum of a wind generated sea as determined from data obtained by the Stereo Wave Observation Project. Meteorological Papers, Vol. 2, University Publishers Tech. Rep., New York University, 88 pp.

Donelan, M. A., J. Hamilton, and W. H. Hui, 1985: Directional spectra of wind-generated waves. *Philos. Trans. Roy. Soc. London,* **A315,** 509–562.

Ewans, K. C., 1998: Observations of the directional spectrum of fetch-limited waves. *J. Phys. Oceanogr.*, **28,** 495–512.

Forristall, G. Z., 1981: Measurements of a saturated range in ocean wave spectra. *J. Geophys. Res.*, **86,** 8075–8084.

——, and K. C. Ewans, 1998: Worldwide measurements of directional wave spreading. *J. Atmos. Oceanic Technol.*, **15,** 440–469.

Hasselmann, D. E., M. Dunckel, and J. A. Ewing, 1980: Directional wave spectra observed during JONSWAP 1973. *J. Phys. Oceanogr.,* **10,** 1264–1280.

Hwang, P. A., 1997: A study of the wavenumber spectra of short water waves in the ocean. Part II: Spectral model and mean square slope. *J. Atmos. Oceanic Technol.,* **14,** 1174–1186.

——, S. Atakturk, M. A. Sletten, and D. B. Trizna, 1996: A study of the wavenumber spectra of short water waves in the ocean. *J. Phys. Oceanogr.,* **26,** 1266–1285.

——, E. J. Walsh, W. B. Krabill, R. N. Swift, S. S. Manizade, J. F. Scott, and M. D. Earle, 1998: Airborne remote sensing applications to coastal wave research. *J. Geophys. Res.,* **103,** 18 791–18 800.

——, D. W. Wang, E. J. Walsh, W. B. Krabill, and R. N. Swift, 2000a: Airborne measurements of the wavenumber spectra of ocean surface waves. Part II. Directional distribution. *J. Phys. Oceanogr.,* **30,** 2768–2787.

——, E. J. Walsh, W. B. Krabill, and R. N. Swift, 2000b: Airborne scanning lidar measurement of ocean waves. *J. Remote Sens. Env.,* **73,** 236–246.

Jackson, F. C., W. T. Walton, and C. Y. Peng, 1985: A comparison of in situ and airborne radar observations of ocean wave directionality. *J. Geophys. Res.,* **90,** 1005–1018.

Kahma, K. K., 1981: A study of the growth of the wave spectrum with fetch. *J. Phys. Oceanogr.,* **11,** 1503–1515.

Kawai, S., K. Okuda, and Y. Toba, 1977: Field data support of three-seconds power law and $gu_*\sigma^4$ spectral form for growing wind waves. *J. Oceanogr. Soc. Japan,* **33,** 137–1515.

Komen, G. J., S. Hasselmann, and K. Hasselmann, 1984: On the existence of a fully developed wind–sea spectrum. *J. Phys. Oceanogr.,* **14,** 1271–1285.

Kondo, J., Y. Fujinawa, and G. Naito, 1973: High-frequency components of ocean waves and their relation to the aerodynamic roughness. *J. Phys. Oceanogr.,* **3,** 197–202.

Krabill, W. B., and C. F. Martin, 1987: Aircraft positioning using global positioning system carrier phase data. *Navigation,* **34,** 1–21.

——, R. H. Thomas, K. Jezek, C. Kuivinen, and S. Manizade, 1995a: Greenland ice sheet thickness changes measured by laser altimetry. *Geophys. Res. Lett.,* **22,** 2341–2344.

——, ——, C. F. Martin, R. N. Swift, and E. B. Frederick, 1995b: Accuracy of airborne laser altimetry over the Greenland ice sheet. *Int. J. Remote Sens.,* **16,** 1211–1222.

Mitsuyasu, H., and Coauthors, 1975: Observation of the directional wave spectra of ocean waves using a cloverleaf buoy. *J. Phys. Oceanogr.,* **5,** 750–760.

——, and Coauthors, 1980: Observations of the directional spectra of ocean waves using a cloverleaf buoy. *J. Phys. Oceanogr.,* **10,** 286–296.

Phillips, O. M., 1958: On some properties of the spectrum of wind-generated ocean waves. *J. Mar. Res.,* **16,** 231–240.

——, 1977: *The Dynamics of the Upper Ocean.* 2d ed. Cambridge University Press, 336 pp.

——, 1985: Spectral and statistical properties of the equilibrium range in wind-generated gravity waves. *J. Fluid Mech.,* **156,** 505–531.

Pierson, W. J., and L. Moskowitz, 1964: A proposed spectral form for fully-developed wind seas based on the similarity theory of S. A. Kitaigorodskii. *J. Geophys. Res.,* **69,** 5181–5190.

Thornton, E. B., and R. T. Guza, 1983: Transformation of wave height distribution. *J. Geophys. Res.,* **88,** 5925–5938.

Toba, Y., 1973: Local balance in the air–sea boundary processes. III. On the spectrum of wind waves. *J. Phys. Oceanogr.,* **3,** 579–593.

——, K. Okada, and I. S. F. Jones, 1988: The response of wind-wave spectra to changing winds. Part 1. Increasing winds. *J. Phys. Oceanogr.,* **18,** 1231–1240.

Walsh, E. J., D. W. Hancock, D. E. Hines, R. N. Swift, and J. F. Scott, 1985: Directional wave spectra measured with the surface contour radar. *J. Phys. Oceanogr.,* **15,** 566–592.

——, ——, ——, ——, and ——, 1989: An observation of the directional wave spectrum evolution from shoreline to fully developed. *J. Phys. Oceanogr.,* **19,** 670–690.

Wyatt, L. R., 1995: The effect of fetch on the directional spectrum of Celtic Sea storm waves. *J. Phys. Oceanogr.,* **25,** 1550–1559.

Young, I. R., 1994: On the measurement of directional wave spectra. *Appl. Ocean Res.,* **16,** 283–294.

——, 1999: *Wind Generated Ocean Waves.* Elsevier, 288 pp.